energies

MDPI

Article

Piezoelectric Energy Harvesting Gyroscopes: Comparative Modeling and Effectiveness

Manuel Serrano [1], Kevin Larkin [2], Sergei Tretiak [2] and Abdessattar Abdelkefi [1,*]

[1] Department of Mechanical and Aerospace Engineering, New Mexico State University, Las Cruces, NM 88003, USA
[2] Los Alamos National Laboratory, Los Alamos, NM 87547, USA
* Correspondence: abdu@nmsu.edu; Tel.: +1-575-646-6546

Abstract: Given its versatility in drawing power from many sources in the natural world, piezoelectric energy harvesting (PEH) has become increasingly popular. However, its energy harvesting capacities could be enhanced further. Here, a mathematical model that accurately simulates the dynamic behavior and energy harvested can facilitate further improvements in the performance of piezoelectric devices. One of the goals of this study is to create a dependable reduced-order model of a multi-purpose gyroscope. This model will make it possible to compute the harvested voltage and electrical power in a semi-analytical manner. The harvested voltage is often modeled as an average value across the whole electrode surface in piezoelectric devices. We propose a model which provides practical insights toward optimizing the performance of the system by considering a spatially varying electric field across the electrode surface length. Our framework allows investigation of the limits of applicability of the modeling assumptions across a range of load resistances. The differential quadrature method (DQM) provides the basis for the suggested numerical solution. The model is also employed to examine energy harvesting under various resistance loads. The newly developed spatially varying model is evaluated for open- and closed-circuit conditions and is proved to be accurate for various values of load resistance that have not previously been considered. The results show that using a spatially varying model is more versatile when modeling the performance of the piezoelectric multifunctional energy harvester. The performance may be accurately captured by the model for load resistances ranging between 10^3 Ω and 10^8 Ω. At optimum load resistance and near 65 KHz, the maximum power output predicted by the spatially varying (SV) model is 1.3 mV, 1.5 mV for the open-circuit (OC) model, and 2.1 mV for the closed circuit (CE) model. At a high-load resistance, the SV and OC models all predict the maximum power output to be 1.9 mV while the CE model predicted the maximum voltage to be 3 mV.

Keywords: piezoelectricity; vibration energy harvesting; electromechanical modeling; gyroscopes

Citation: Serrano, M.; Larkin, K.; Tretiak, S.; Abdelkefi, A. Piezoelectric Energy Harvesting Gyroscopes: Comparative Modeling and Effectiveness. *Energies* **2023**, *16*, 2000. https://doi.org/10.3390/en16042000

Academic Editors: Wael A. Altabey and Sallam A. Kouritem

Received: 7 January 2023
Revised: 9 February 2023
Accepted: 14 February 2023
Published: 17 February 2023

1. Introduction

Harvesting energy allows for the repurposing of otherwise lost resources [1]. Today, many cutting-edge electronics can be powered by using the collected energy that would otherwise be lost [2,3]. Common energy harvesting methods rely on the concepts of piezoelectricity, electromagnetics, triboelectricity, photovoltaics, thermoelectricity, and electrostatics. Micro-/nano-scale processes find particular utility in piezoelectric, triboelectric, and electrostatic energy harvesting methods [4]. Certain materials referred to as piezoelectric materials exhibit a sort of interaction between their mechanical and electrical properties that is known as piezoelectricity. When subjected to a mechanical strain, piezoelectric materials exhibit a basic phenomenon known to produce an electric charge. Increased levels of stress almost always result in increased levels of potential or voltage. In nature, several crystals have been observed to exhibit the piezoelectric effect, such as

Rochelle salt, quartz, and topaz. However, the research suggests that piezoceramics, such as PZT, are the materials that see the most widespread application [5–11].

The method of piezoelectric energy harvesting is extremely flexible since it may make use of a wide variety of environmental factors for the production of power [12–19]. Tan et al., in a recent study, looked into the benefits of coupling piezoelectric galloping energy harvesting with the natural environment [20]. By utilizing vortex-induced vibrations [20–26] and galloping, the harvesters generated more energy [21,27–31]. Furthermore, PEH have been studied for their possible application in devices that harness energy from human movements [32–37]. Technologies based on these principles have shown a lot of promise in the areas of wireless and remote sensing and wearable health devices, all of which require small, portable sources of power [23,24,38–41], space, military applications, and microelectromechanical (MEMS) technologies [42–45]. Modeling multifunctional systems that are also capable of harvesting energy has become of great recent interest to researchers [46]. For instance, by using a lattice sandwich beam, a nonlinear energy sink (NES), and a giant magnetostrictive material (GMM), Zhang et al. [47] proposed a novel multifunctional lattice sandwich structure. As demonstrated by their findings, this novel multifunctional lattice sandwich construction was capable of producing the intended multifunctional effect of vibration reduction and energy harvesting. Similarly, Brito-Pereira et al. [48] investigated a magnetically activated system with sensing and energy harvesting capabilities. In addition to sensing magnetic fields, the magnetoactive device also has the capabilities of harvesting magnetic energy. A recent study by Cho et al. [49] presented a road-compatible piezoelectric energy harvester (RPEH) that harnesses energy to power independent sensors and car indicators. Tests of the RPEH module indicate its capability to monitor temperature, strain, and leakage data in real time, and the produced energy is adequate to light LED indicators. In addition, it was discovered that piezoelectric devices deliver high output power with minimum vertical displacement, making them very efficient and robust for practical highway energy-harvesting applications.

In contrast to the practice of using a constant electric field in modeling energy harvesting microgyroscopes, the primary objective of this research is placed on implementing spatially varying electric fields instead. In this work, we introduce a novel model considering the variation of the electric field with the beam's length to accurately calculate the harvested electrical power across a wide range of load resistances. The extended Hamilton's principle is applied to derive the equations of motion and boundary conditions from the kinetic and potential energies of the system and the Differential Quadrature Method (DQM) is implemented to discretize these equations. The DQM is a relatively recent technique that is gradually gaining popularity [42,50,51] as a separate methodology for solving problems in the physical and engineering sciences [52–55]. Our approach is compared with three other models to determine the limits of applicability and other factors, such as reducing complexity and simulation time.

In this study, a piezoelectric patch is incorporated into a MEMS gyroscope such that it may perform two functions at the same time: collecting energy through the piezoelectric effect and monitoring changes in angular velocity. This paper is constructed as follows: Section 1 delineates four separate state-of-the-art models for gyroscopes with energy harvesting capabilities. In Section 2, the reduced-order model that describes the physics of the system is formulated. Finally, Section 3 compares the four models against each other for different parameters, such as load resistance, AC voltage, and base rotation.

2. Modeling of Energy Harvesting Microgyroscope

A schematic representation of the cantilever beam-type energy-harvesting gyroscope system that is under study is presented in Figure 1. To activate the beam, DC and AC voltages are implemented to actuated the beam in the driving direction. A piezoelectric patch is positioned on the sensing side of the nanocrystalline silicon beam. When the gyroscope's base rotates, the resulting Coriolis force causes the beam to vibrate in the

sensing direction. Measuring the voltage created by the piezoelectric layer allows one to compute the angular velocity of the gyroscope system.

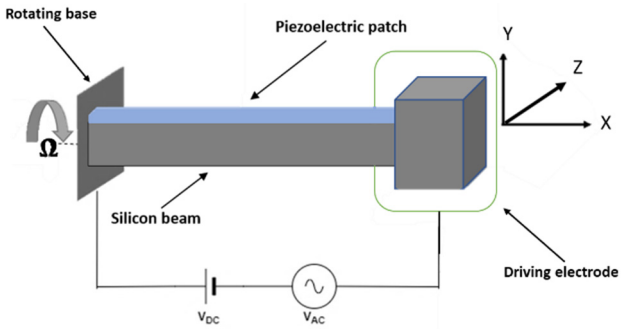

Figure 1. Schematics of gyroscope sensor with energy harvesting capabilities.

2.1. Microgyroscope Energy Harvesting: Governing Equations of Motion

Layers of silicon and piezoelectric material make up the cantilever beam's construction. The whole beam's sensing surface is covered with a bonded piezoceramic patch with dimensions L_p, b_p and h_p while the beams length, width, and thickness are denoted as L, b_s, h_s. Following the work of Lajimi et al. [43,44], the total kinetic energy is expressed as:

$$\begin{aligned} K = \int_0^L \Big(& \tfrac{1}{2} m\Omega^2 (v^2 + w^2) + m\Omega(v\dot{w} - w\dot{v}) + \tfrac{1}{2} j_y \dot{v}'^2 + \tfrac{1}{2} j_z \dot{w}'^2 \\ & + \Omega j_z \left(v'\dot{w}' + w'\dot{v}' \right) + \tfrac{1}{2} m \left(\dot{v}^2 + \dot{w}^2 \right) \\ & - \tfrac{1}{2}\Omega^2 \left(j_z \left(w'^2 - 1 \right) + j_y \left(v'^2 - 1 \right) \right) \Big) dx \\ & + \tfrac{M}{2} \left(\dot{v}_L^2 + \dot{w}_l^2 + 2 v_L \dot{w}_L \Omega - 2 w_L \dot{v}_L \Omega + v_L^2 \Omega^2 \right. \\ & \left. + w_L^2 \Omega^2 \right) \end{aligned} \tag{1}$$

The parameter associated with v is the deflection in the sensing direction, w denotes the deflection in the driving direction, and parameters v_L and w_L represent the sensing and driving deflections at $x = L$, respectively. The spatial and time derivatives are denoted by primes, $(\,)'$, and with dots, $\dot{(\,)}$, respectively. Moreover, m (Equation (2)) stands for the beam's mass divided by its length and is written as:

$$m = \rho_p b_p h_p + \rho_s b_s h_s \tag{2}$$

Following [56,57], the potential energies for the beam and the electrostatic force (Equation (3a,b)) can be expressed as:

$$U = \frac{1}{2} \left(\int_0^L \int_{A_s} \sigma_{11}^s \epsilon_{11} dA_s dx + \int_0^L \int_{A_s} \sigma_{11}^p \epsilon_{11} dA_p dx - \int_0^L \int_{A_p} E_3 D_3 dA_p dx \right) \tag{3a}$$

$$\delta U_e = -\frac{\epsilon A_w (V_{DC} + v_{AC}(t))^2}{2} \left(\frac{1}{(d_w - w_L)^2} + \frac{0.65}{b_m (d_w - w_L)} \right) \delta w_L \tag{3b}$$

In this context, the cross-sectional area of the piezoelectric patch and the silicon beam are referred to by their respective abbreviations, A_s and A_p. The strain, ϵ_{11}, and stresses, σ_{11}^s and σ_{11}^p, in the silicon and piezoelectric layers are connected as follows (Equation (4)) when the linear constitutive equations of piezoelectricity are used [58]:

$$\sigma_{11}^s = E_s \epsilon_{11} \text{ and } \sigma_{11}^p = E_p \epsilon_{11} - e_{31} E_3 \tag{4}$$

Here, the modulus of elasticity of the silicon and piezoelectric layers, E_S and E_p, are depicted by their respective variable names. It is possible to define the electric field, denoted by E_3, in terms of the electric potential difference:

$$E_3(x,t) = -\frac{V(x,t)}{b_p} \tag{5}$$

where $V(x,t)$ is the voltage across the resistive load. The expression for the electric displacement, D_3, can then be formulated as follows [1]:

$$D_3 = e_{31}\epsilon_{11} + \in_{33}^{s} E_3 \tag{6}$$

where e_{31} is the piezoelectric stress coefficient and $\in_{33}^{s}$ denotes the dielectric permittivity at a constant axial strain. Due to the asymmetric geometrical and material properties of the gyroscope, it is necessary to determine the position of the neutral axis, $\overline{y}$. In relation to the location of the neutral axis, denoted by $\overline{y}$, the locations of the beam and the piezoelectric layers, as illustrated in Figure 2, are determined as follows:

$$y_o = -\overline{y}\; y_1 = b_s - \overline{y}\;;\; y_2 = \left(b_p + b_s\right) - \overline{y} \tag{7}$$

$$\overline{y} = \frac{\left(b_p + b_s\right) E_p\; b_p}{2\left(E_p b_p + E_s b_s\right)} + \frac{1}{2} b_s \tag{8}$$

The boundaries associated with the width of the beam and piezoelectric layer are denoted by y_o, y_1, and y_2.

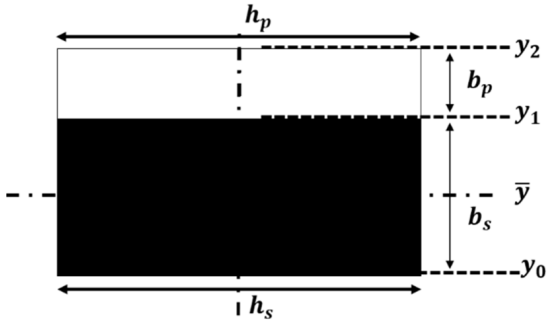

Figure 2. Neutral axis position for the beam section covered with the piezoelectric material.

We may write the potential energy of the system using Equations (5)–(7), which is:

$$\begin{aligned} U = \tfrac{1}{2}\int_0^L \left[EI_v v''^2\right]dx + \tfrac{1}{2}\int_0^L \left[EI_w w''^2\right]dx - \int_0^L \tfrac{(y_2+y_1)}{2} h_p e_{31} V(x,t) v''\, dx \\ -\tfrac{1}{2}\int_0^L \tfrac{\in_{33}^{s} h_p}{b_p}\, V^2(x,t)dx \end{aligned} \tag{9}$$

where the mechanical stiffnesses, EI_v and EI_w, are given by:

$$EI_v = \frac{y_1^3 - y_0^3}{3} h_s E_s + \frac{y_2^3 - y_1^3}{3} h_p E_p \tag{10}$$

$$EI_w = \frac{y_1 - y_0}{12} h_s^3 E_s + \frac{y_2 - y_1}{12} h_p^3 E_p \tag{11}$$

The relationship between the voltage produced and the extracted charge is as follows:

$$V(x,t) = R\frac{\delta Q(x,t)}{\delta t} \tag{12}$$

Work carried out that is not considered conservative may be broken down into two categories: the work that is conducted by the power that is given to the electrical circuit, and work that is conducted by the viscous damping force. The expression for the non-conservative work term is as follows:

$$\delta W_{nc} = -\int_0^L V(x,t)\delta Q(x,t)dx - \int_0^L c\dot{v}\delta v dx \tag{13}$$

An Euler–Bernoulli beam is designated to represent the reaction of the energy harvester. In order to calculate the equations of motion and the boundary conditions that correspond to them, the extended Hamilton's principle is utilized:

$$\int_{t_1}^{t_2}(\delta T - \delta U - \delta U_e + \delta W_{nc})dt = 0 \tag{14}$$

Given below are the governing equations of motion and boundary conditions, which from here on out will be referred to as the spatially varied model (SV):

$$EI_v v^{iv} - m\ v\Omega^2 - j_v\Omega^2 v'' - 2m\ \Omega\dot{w} + m\ \ddot{v} - j_v\ddot{v}'' + c_v\dot{v} + \theta V''(x,t) = 0 \tag{15}$$

$$EI_w w^{iv} - m\ w\Omega^2 - j_w\ \Omega^2 w'' + 2m\ \Omega\dot{v} + m\ \ddot{w} - j_w\ddot{w}'' + c_w\dot{w} = 0 \tag{16}$$

$$-e_{31}h_p\frac{y_2+y_1}{2}\dot{v}'' - \frac{\varepsilon_{33}h_p\dot{V}(x,t)}{bp} - \frac{V(x,t)}{LR} = 0 \tag{17}$$

The accompanying boundaries are:

$$v(0,t) = w(0,t) = 0\ ;\ v'(0,t) = w'(0,t) = 0;\ V(0,t) = 0 \tag{18}$$

$$v''(L,t) = w''(L,t) = 0; V(L,t) = 0 \tag{19}$$

$$EI_v v'''(L,t) + M\Omega^2 v(L,t) + 2M\Omega\dot{w}(L,t) - M\ddot{v}(L,t) - j_v\Omega^2 v'(L,t) - j_v\ddot{v}'(L,t) = 0 \tag{20}$$

$$\begin{gathered} EI_w w'''(L,t) + M\Omega^2 w(L,t) - 2M\Omega\dot{v}(L,t) - M\ddot{w}(L,t) - j_w\Omega^2 w'(L,t) - j_w\ddot{w}'(L,t) = \\ -\frac{\epsilon A_w(V_{DC}+v_{AC}(t))^2}{2}\left(\frac{1}{(d_w - w(L,t))^2} + \chi\frac{0.65}{b_m(d_w - w(L,t))}\right) \end{gathered} \tag{21}$$

where any subscripts with v and w denote parameter quantities in the sensing or driving directions, respectively. A gap of width d_w separates the electrode from the beam. A_w and ϵ denotes the electrode area and electrical permittivity, respectively. The parameter M, denoted the tip mass, and width, denoted by the value b_m, are both characteristics of the tip mass. The mass moment of inertia in the driving direction is denoted by j_w, while the mass moment of inertia in the sensing direction is denoted by j_v, while the angular rotation is denoted by Ω. The expressions j_w and j_v are as follows:

$$j_w = \frac{\rho(y_1 - y_0)h^3}{12} + \frac{\rho_p(y_2 - y_1)h_p^3}{12} \text{ and } j_v = \frac{\rho\left(y_1^3 - y_0^3\right)h}{3} + \frac{\rho_p\left(y_2^3 - y_1^3\right)h_p}{3} \tag{22}$$

The actuation voltage, $v_{AC}(t) = V_{AC}\sin(\omega_e t)$ is the component of the electrical force that is responsible for the beam actuation, and the excitation frequency is denoted by ω_e. By incorporating the following parameters below, the equations of motion and boundary conditions may be transformed into a dimensionless form.

$$\begin{gathered} \hat{x} = \frac{x}{L}\ ;\ \hat{v} = \frac{v}{d_w};\ \ \hat{w} = \frac{w}{d_w};\ \tau = \sqrt{\frac{D_v}{mL^4}}\ ;\ \ \hat{\Omega} = \frac{\Omega}{\tau}\ ;\ \ J_w = \frac{j_w}{m\ L^2}\ ;\ J_v = \frac{j_v}{m\ L^2}\ ;\ \hat{t} = \tau t\ ;\ M_r = \frac{M}{m\ L} \\ D_{wr} = \frac{D_w}{D_v}; x = \frac{\hat{x}}{L}; \hat{V} = \frac{V}{V_n}; V_n = \frac{\theta g}{LCp}; \theta = -e_{31}h_p\frac{y_2+y_1}{2}\ \gamma = \frac{\theta^2 L}{C_p D_v}; C_p = \frac{\varepsilon_{33}h_p L}{b_p} \end{gathered} \tag{23}$$

The ˆ represents dimensionless values. In the remaining equations, the ˆ is removed to simplify the notation. The following are the dimensionless equations of motion and boundary conditions for the SV model:

$$v^{iv} - \Omega^2 v - J_v \Omega^2 v'' - 2\Omega \dot{w} + \ddot{v} - J_v \ddot{v}'' + \mu_v \dot{v} + \gamma V''(x,t) = 0 \tag{24}$$

$$D_{wr} w^{iv} - \Omega^2 w - J_w \Omega^2 w'' + 2\Omega\ \dot{v} + \ddot{w} - J_w \ddot{w}'' + \mu_w \dot{w} = 0 \tag{25}$$

$$\dot{v}''(x,t) - \dot{V}(x,t) - \frac{V(x,t)}{R\tau C_p} = 0 \tag{26}$$

Then, the dimensionless boundary conditions are expressed as:

$$v(0,t) = w(0,t) = 0;\ v'(0,t) = w'(0,t) = 0;\ V(0,t) = 0 \tag{27}$$

$$v''(1,t) = w''(1,t) = 0;\ V(1,t) = 0 \tag{28}$$

$$v'''(1,t) + M_r \Omega^2 v(1,t) - J_v \Omega^2 v'(1,t) + 2M_r \Omega \dot{w}(1,t) - M_r \ddot{v}(1,t) - J_v\ \ddot{v}'(1,t) = 0 \tag{29}$$

$$\begin{aligned} D_{wr} w'''(1,t) + M_r \Omega^2 w(1,t) - J_w \Omega^2 w'(1,t) - 2M_r \Omega\ \dot{v}(1,t) - M_r \ddot{w}(1,t) - J_w \ddot{w}'(1,t) = \\ -\frac{\epsilon_0 A_w L^3 (V_{DC} + v_{AC}(t))^2}{2D_v d_v} \left(\frac{1}{d_w^2 (1 - w(1,t))^2} + \chi \frac{0.65}{d_w b_m (1 - w(1,t))} \right) \end{aligned} \tag{30}$$

The boundary conditions for the four models, Equations (27)–(30), remain the same so that they are not repeated in the mathematical equations of the remaining model sections. Only the differences between the models will be highlighted in the equations of motion.

2.1.1. Open-Circuit (OC) Modeling

It is possible to lessen the complexity of the SV model by lowering the number of coupling terms that exist between the energy harvesting circuit and the mechanical structure of the beam. It is possible to establish what is known as an open-circuit model (OC) by making the assumption that the load resistance, R, is indefinitely large. Reducing Equation (26) to:

$$v''(x,t) = V(x,t) \tag{31}$$

The following equations of motion are obtained by substituting Equation (31) into Equation (24), and the governing equations can be expressed as:

$$(\gamma + 1) v^{iv} - \Omega^2 v - J_v \Omega^2 v'' - 2\Omega \dot{w} + \ddot{v} - J_v \ddot{v}'' + \mu_v \dot{v} = 0 \tag{32}$$

$$D_{wr} w^{iv} - \Omega^2 w - J_w \Omega^2 w'' + 2\Omega\ \dot{v} + \ddot{w} - J_w \ddot{w}'' + \mu_w \dot{w} = 0 \tag{33}$$

This model includes the voltage effects on the structural components of the system through a backward coupling term in the stiffness parameter in the sensing equation; γ. The OC model can only be considered reliable for extremely high levels of load resistance.

2.1.2. Constant (Average) Electric Field Open Circuit (CE-γ)

The power generated by PEH devices is estimated in the published works by utilizing an average voltage value throughout the full beam length [59–61]. It is assumed that the harvester voltage only varies with time, $V(t)$. For this model, called the CE-γ model, the Gauss law Equation (26) is reduced to an ODE Equation (34) and some load resistance effects beyond those exhibited in the open-circuit model, are captured in the voltage calculation. Equation (34), which describes the open-circuit configuration coupling in the sensing direction, helps the CE-γ model achieve a higher degree of precision for significantly greater levels of load resistance. The governing equations that result from applying this modeling method are as follows:

$$\dot{v}'(1\ ,t) - \dot{V}(t) - \frac{V(t)}{R\tau C_p} = 0 \tag{34}$$

$$(\gamma+1)v^{iv} - \Omega^2 v - J_v\Omega^2 v'' - 2\Omega\dot{w} + \ddot{v} - J_v\ddot{v}'' + \mu_v\dot{v} = 0 \tag{35}$$

$$D_{wr}w^{iv} - \Omega^2 w - J_w\Omega^2 w'' + 2\Omega\ \dot{v} + \ddot{w} - J_w\ddot{w}'' + \mu_w\dot{w} = 0 \tag{36}$$

2.1.3. Constant (Average) Electric Field (CE)

After deleting the coupling element from the sensing equation of motion, one may arrive at the following formulation for a short-circuit configuration of the average electric field model:

$$\dot{v}'(1\ ,t) - \dot{V}(1,t) - \frac{V(t)}{R\tau C_p} = 0 \tag{37}$$

$$v^{iv} - \Omega^2 v - J_v\Omega^2 v'' - 2\Omega\dot{w} + \ddot{v} - J_v\ddot{v}'' + \mu_v\dot{v} = 0 \tag{38}$$

$$D_{wr}w^{iv} - \Omega^2 w - J_w\Omega^2 w'' + 2\Omega\ \dot{v} + \ddot{w} - J_w\ddot{w}'' + \mu_w\dot{w} = 0 \tag{39}$$

This model, referred to hereafter as CE, only holds true for relatively low load resistances. Table 1 summarizes the four models and the assumptions upon which they are based.

Table 1. Summary of models.

Model	Voltage Representation	Voltage Coupling	Voltage Coupling in Sensing E.O.M
SV	Spatially varying electric field	Resistance dependent	Backward coupling (resistance-dependent voltage term)
OC	Spatially varying electric field	Open circuit ($R = \infty$)	Backward coupling (open-circuit voltage)
CE-γ	Constant (average) electric field	Open circuit ($R = \infty$)	Backward coupling (open-circuit voltage)
CE	Constant (average) electric field	Short circuit ($R = 0$)	None

2.2. Static and Eigenvalue Problem Analyses of the Multifunctional Microgyroscope

The static pull-in is a phenomenon that occurs when the structural restoring force cannot withstand the electrostatic force causing the gyroscopic beam to collapse onto the driving electrode. It is extremely important to identify the DC voltages at which pull-in occurs, so the proper operation of the gyroscope is ensured. The static behavior of the decoupled system is vitally important to the overall design and operation of the microgyroscope. Eliminating all time-dependent variables from the driving equation of motion allows us to derive the static deflection in the driving direction. The equation with the reductions may be written as:

$$w_s^{iv}(x) = 0 \tag{40}$$

with the accompanying stipulations:

$$w_s(0) = 0;\ w_s'(0) = 0 \tag{41}$$

$$w_s''(1) = 0 \tag{42}$$

$$w_s'''(1) = -\frac{\epsilon_0 A_w L^3 V_{DC}^2}{2D_v d_w}\left(\frac{1}{d_w^2(1-w_s)^2} + \chi\frac{0.65}{d_w b_m(1-w_s)}\right) \tag{43}$$

The general solution for w_s is:

$$w_s(x) = A + Bx + Cx^2 + Dx^3 \tag{44}$$

It is then possible to quantitatively derive the values of A, B, C, and D by making use of the boundary conditions. Operating near resonance is recommended to amplify the microbeam motion in the sense direction [38] and to achieve a larger output signal. The work carried out by Ghommem et al. [38] is used as a reference for the purpose of determining the inherent frequencies of the system and defining the eigenvalue problem. The microbeam's deflection may be calculated by adding the static and dynamic components together:

$$v(x,t) = v_s(x) + \left(\phi_v(x)e^{i\omega t} + cc\right) \tag{45}$$

$$w(x,t) = w_s(x) + \left(\phi_w(x)e^{i\omega t} + cc\right) \tag{46}$$

where $\phi_v(x)$ and $\phi_w(x)$ are the mode shapes of the microbeam in the sense and drive directions, respectively. ω denotes the natural frequencies while cc is short for the complex conjugate of the preceding term. The spatial functions $\phi_v(x)$ and $\phi_w(x)$ have the following form:

$$\phi_v(x) = \sum_{i=1}^{8} (\phi_{v,i})e^{s_i x} \tag{47}$$

$$\phi_w(x) = \sum_{i=1}^{8} (\phi_{w,i})e^{s_i x} \tag{48}$$

The gyroscope's vibrational equations and boundary conditions are obtained by inserting Equations (47) and (48) into Equations (24)–(30) and extending the electrostatic force term using the Taylor series expansion to produce its linear expression:

$$\left[s^4 N_1 + s^2 N_2 - N_3\right] \begin{Bmatrix} \phi_{v,i} \\ \phi_{w.i} \end{Bmatrix} \tag{49}$$

where

$$N_1 = \begin{bmatrix} 1 & 0 \\ 0 & D_{wr} \end{bmatrix} \tag{50}$$

$$N_2 = \begin{bmatrix} J_v\omega^2 - J_v\Omega^2 & 0 \\ 0 & J_w\omega^2 - J_w\Omega^2 \end{bmatrix} \tag{51}$$

$$N_3 = \begin{bmatrix} \omega^2 + \Omega^2 & 2i\omega\Omega \\ -2i\omega\Omega & \omega^2 + \Omega^2 \end{bmatrix} \tag{52}$$

$$\phi_{v,i}(0) = \phi_{w,i}(0) = 0;\ \phi_{v,i}{}'(0) = \phi_{w,i}{}'(0) = 0;\ V(0) = 0 \tag{53}$$

$$\phi_{v,i}{}''(1) = \phi_{w,i}{}''(1) = 0;\ V(1) = 0 \tag{54}$$

$$\phi'''_{v,i}(1) + M_r\Omega^2\phi_{v,i}(1) - J_v\Omega^2\phi'_{v,i}(1) + 2M_r\Omega\dot{\phi}_{w,i}(1) - M_r\ddot{\phi}_{v,i}(1) - J_v\,\ddot{\phi}_{v,i}{}'(1) = 0 \tag{55}$$

$$\begin{aligned} D_{wr}\phi'''_{w,i}(1) + M_r\Omega^2\phi_{w,i}(1) - J_w\,\Omega^2\phi'_{w,i}(1) - 2M_r\Omega\,\dot{\phi}_{v,i}(1) - M_r\ddot{\phi}_{w,i}(1) - J_w\,\ddot{\phi}_{w,i}{}'(1) = \\ -\frac{\epsilon_0 A_w L^3 (V_{DC}+v_{AC}(t))^2}{2D_v d_v}\left(\frac{1}{d_w^2(1-w_s(1))^2} + \chi\frac{0.65}{d_w b_m(1-w_s(1))}\right)\phi_{w,i}(1) \end{aligned} \tag{56}$$

It is possible to compile the boundary conditions into an 8×8 matrix, the elements of which are solely determined by the beam's natural frequency. When the determinant of the resulting matrix is set to zero, the corresponding natural frequencies may be calculated. Figure 3 shows the initial natural frequency of the EHMG for increasing the DC voltages. Note the "sense mode γ" curve represents the sensing natural frequency when coupled with the backward coupling term in the stiffness parameter.

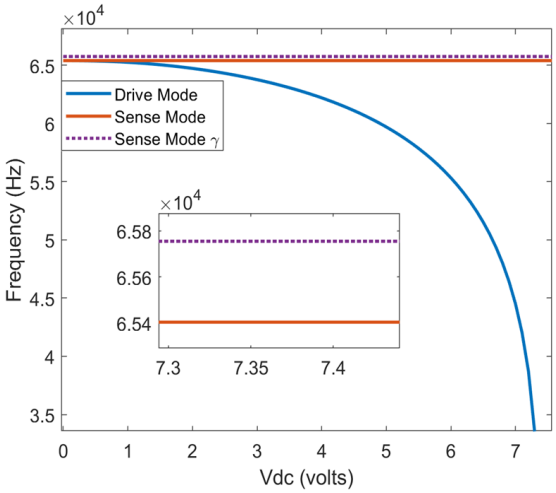

Figure 3. Coupled frequencies of the microgyroscope $\Omega = 80$ rad/s.

2.3. Differential Quadrature Method (DQM)

The differential quadrature approach has been shown to provide extremely accurate results with little computing cost [42]. Potentially replacing established approaches to the numerical solution, such as the finite difference and finite element methods, the method shows promise. [42,50,51]. The energy harvester is modeled as a collection of nonlinear PDE's, all of which are unsolvable from an analytical perspective. Therefore, the DQM is employed for spatial discretization of the governing equations. For further details on the DQM methodology, refer to [57].

As shown in a previous study, an accurate solution can be achieved when the number of DQM grid points is set equal to 8 [57]. The evolution of the voltage over time is depicted in Figure 4a, which includes time histories for all models. The voltage across the beam is plotted in Figure 4b. For the CE and CE-γ models, the voltage is shown to be a constant value across the beam while the voltage for the SV and OC models varies with respect to x.

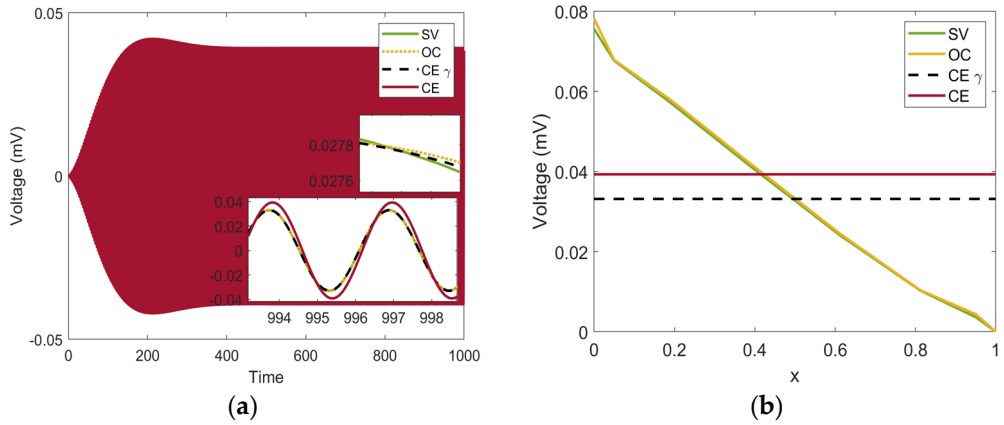

Figure 4. (**a**) Voltage time history and (**b**) voltage with respect to x.

3. Model Comparison and Results

The critical microbeam and piezoelectric parameters are enumerated in Table 2, which offers a condensed overview of their values.

Table 2. Microbeam and piezoelectric parameters [56,57,62].

Parameters	Values	Parameters	Values
Beam length, L	400 µm	Piezoelectric layer thickness, h_p	2.8783 µm
Beam thickness, h_s	2.8783 µm	Piezoelectric layer width, b_p	1 µm
Beam width, b_s	2.5081 µm	Piezoelectric density, ρ_p	5440 kg/m^3
Driving electrode gap, d_w	2 µm	Piezoelectric Young's modulus, E_p	30.336 GPa
Driving capacitor area, A_w	192 µm^2	Vacuum electric permittivity, ϵ_0	8.85×10^{-12} F/m
Tip mass width, b_m	20 µm	Piezoelectric permittivity, ϵ_{33}	12.653×10^{-9} F/m
Piezoelectric layer length, L	400 µm		

A comparison study is carried out for a variety of load resistance values in order to ascertain the applicability limitations that are associated with the various models. Frequency response curves shown in Figures 5–7 depict the displacements and voltage harvested using each modeling technique. We assume 1 V DC and 0.1 V AC, respectively. As can be seen in Figure 5, the magnitude of the load resistance does not have a substantial impact on the driving displacement for any of the models that have been taken into consideration. This is because of the electrostatic forcing in the driving direction and the fact that there is no direct coupling between the driving and voltage equations of motion.

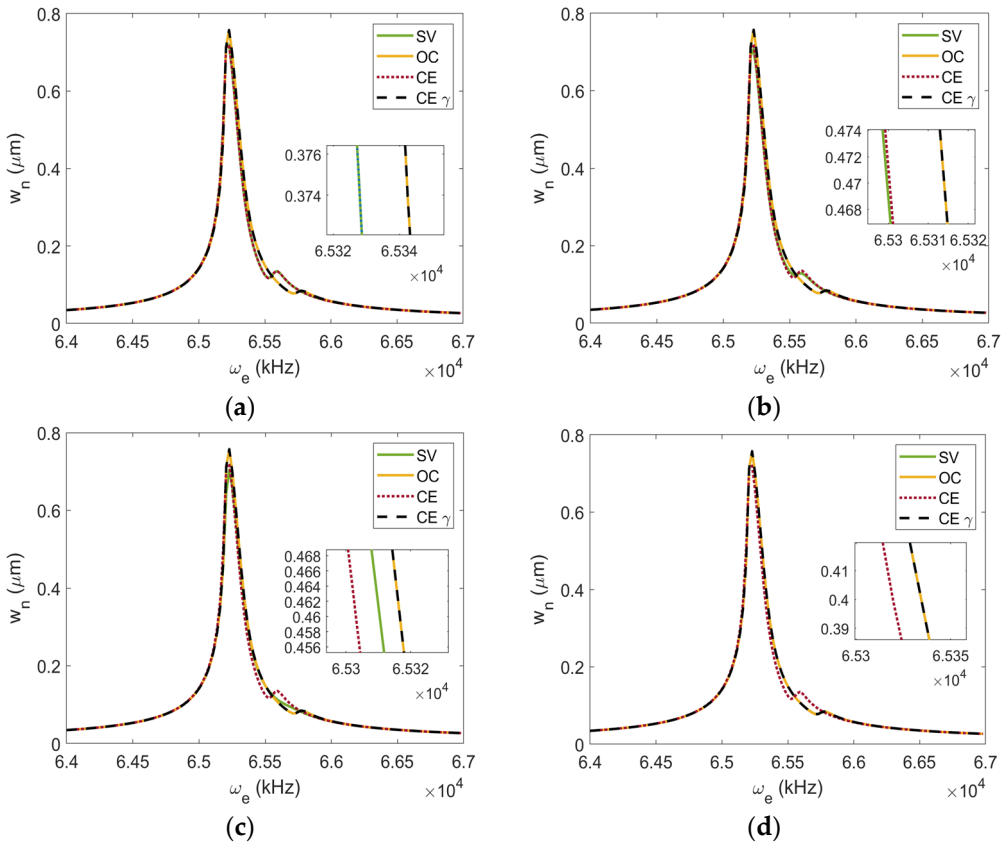

Figure 5. Driving displacement variations as a function of the excitation frequency: (**a**) $R = 10^3\ \Omega$, (**b**) $R = 10^5\ \Omega$, (**c**) $R = \frac{1}{C_p \omega_n}\ \Omega$, and (**d**) $R = 10^8\ \Omega$ when $V_{DC} = 1$ V, $V_{AC} = 0.1$ V, $\Omega = 80\ \frac{\text{rad}}{\text{s}}$, $\mu = 0.01$.

However, we observe a slight difference in the driving response near the sensing frequency. The sensing displacement and voltage deviate greatly based on the chosen modeling technique. Figure 6 illustrates the frequency response of the sensing displacement

for each of the four models at a variety of load resistance levels. This response is shown for each of the four models in the figure. Figure 6a shows the sensing displacement curves for a low value of the load resistance, $R = 10^3\ \Omega$. It is observed that for a near short-circuit scenario, the SV and the CE models mutually converge. In contrast, the OC and CE-γ models agree with each other, but they do not match the SV and CE models. The coupled frequency is responsible for the amplitude gap that exists between the resonance peaks in the sensing response. As can be observed in the frequency response graphs of both the sensing displacement and the produced voltage, which are shown in Figures 6 and 7, the electrical load resistance has a significant impact on the coupled frequency in the sensing direction. The assumptions shown in Table 1 for each model lead to the coupled frequency differences.

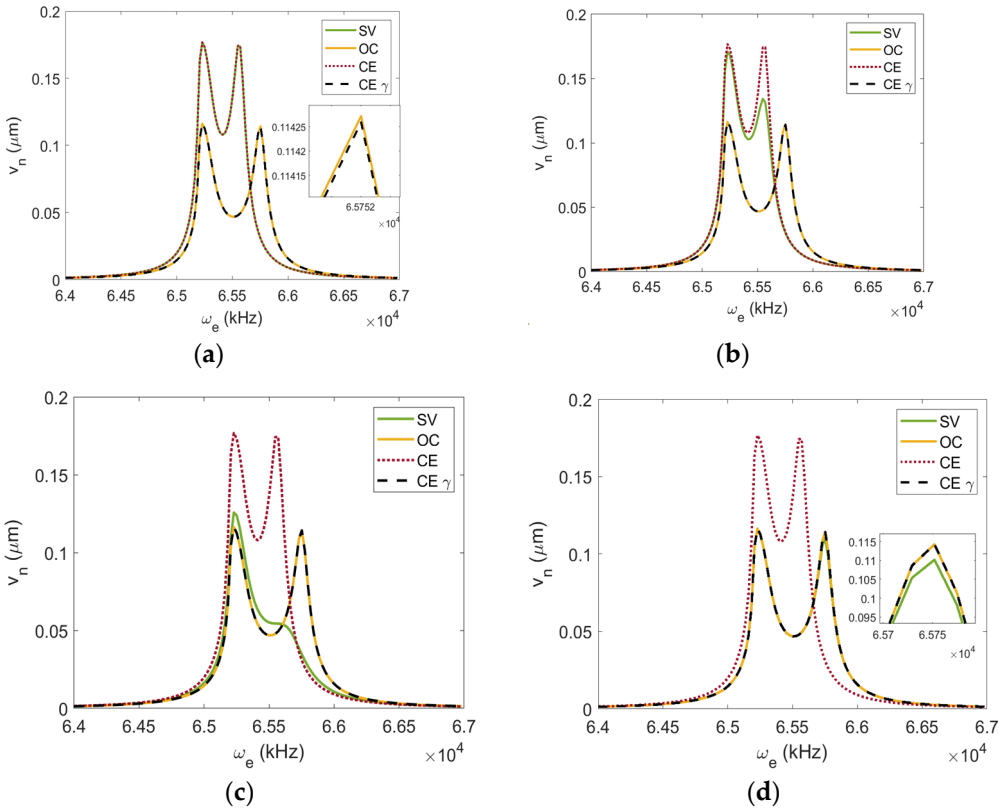

Figure 6. Sensing displacement variations as a function of the excitation frequency: (**a**) $R = 10^3\ \Omega$, (**b**) $R = 10^5\ \Omega$, (**c**) $R = \frac{1}{C_p\omega_n}\ \Omega$, and (**d**) $R = 10^8\ \Omega$ when $V_{DC} = 1$ V, $V_{AC} = 0.1$ V, $\Omega = 80\ \frac{\text{rad}}{\text{s}}$, $\mu = 0.01$.

Figure 7a shows that the output voltage is significantly overestimated by the OC model for a near short-circuit situation, as open-circuit conditions are assumed. When the load resistance is increased to $R = 10^5\ \Omega$, the SV, CE, and CE-γ models feature increases in amplitude because they are approaching optimum load resistance for harvested energy, which can be seen in Figure 7c. Notably, the CE model closely matches the SV model near the driving resonance frequency but falls short near the sensing frequency because of the missing coupling terms in the sensing equation. The most significant difference may be seen between the models when using the load resistance that is considered to be optimal. Here, the CE-γ model closely matches the SV model near the driving resonance frequency but also falls short near the sensing frequency because of the missing coupling terms in the sensing equation. The SV model is dependent on load resistance; hence, it is the only model that can be considered as valid when close to the optimum load resistance. Furthermore, considering a high-load resistance value, $10^8\ \Omega$, the agreement between SV, OC, and CE-γ

models is high. This is due to the fact that, at a high-load resistance, the SV and CE-γ models should be mathematically equivalent to the OC model.

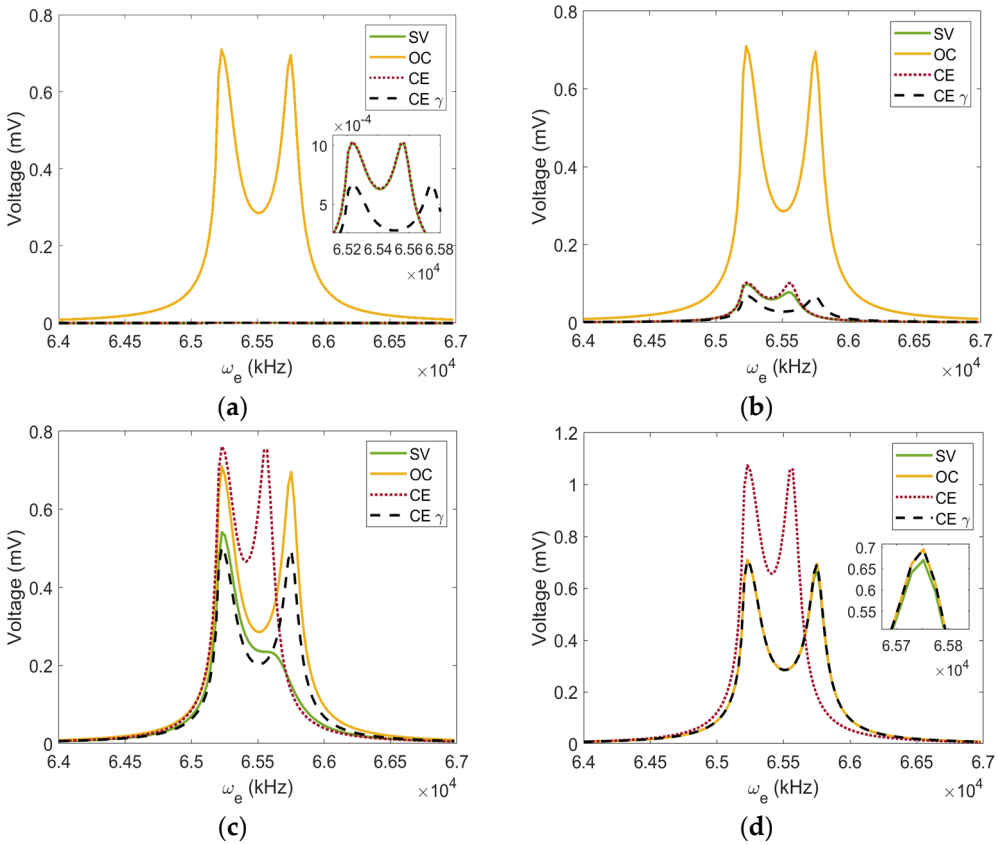

Figure 7. Voltage output variations as a function of the excitation frequency: (**a**) $R = 10^3\ \Omega$, (**b**) $R = 10^5\ \Omega$, (**c**) $R = \frac{1}{C_p \omega_n}\ \Omega$, and (**d**) $R = 10^8\ \Omega$ when $V_{DC} = 1$ V, $V_{AC} = 0.1$ V, $\Omega = 80\ \frac{\text{rad}}{\text{s}}$, $\mu = 0.01$.

Similarly, the frequency response functions in Figures 8–10 consider constant 1V DC and 0.5 V AC, respectively. Figures 8–10 depict the same trend as the lower actuation voltage case. Clearly, from the plotted curves, increasing the AC voltage allows for increased driving and sensing amplitudes. On the other hand, varying the AC voltage does not have a significant influence on the bandwidth; however, an excessive AC voltage can cause dynamic pull-in, which should be avoided. Increasing the AC voltage does not greatly affect the limits of applicability for each model. Using a higher AC voltage does, however, cause dynamic pull-in in the system, which can be seen as discontinuity in the driving, sensing, and voltage-harvested plots. There is no pronounced driving peak in the voltage because of the nonlinear softening.

To obtain the most out of a certain energy harvester design at a given excitation frequency, the optimal value for the electrical load resistance, R, must be found. We further seek the optimal R values of the multifunctional piezoelectric energy harvester, as well as how these values affect the overall performance of the system. Figure 11 illustrates the driving and sensing displacements of the system, as well as the impacts of R on the voltage and power outputs of all four models that are the subject of this investigation. The direct and alternating current voltages are set equal to 1 V and 0.1 V, respectively. We match the driving mode's inherent frequency to the excitation frequency at $V_{DC} = 0$ V ($\omega_e =$ 65 kHz). To validate the models for different load resistances, they are compared with the SV model. For different load resistances, if that model matches up well with the SV model, it can be considered accurate for that load resistance value. In Figure 11a, we can see that the driving displacements of the OC, CE, and CE-γ models are only slightly affected by the electrical load resistance. Only the resistance-dependent model, abbreviated as SV, is

considered to be valid when the load resistance is somewhat close to the optimal load resistance. Observing Figure 11b, the CE model is only valid for short-circuit conditions up to a load resistance of $R \leq 10^4\ \Omega$, while the OC and CE-γ models are only valid for open-circuit conditions or load resistances of $R > 10^8\ \Omega$. This agreement between the OC and CE-γ models with the SV model is due to the shunt-damping effects captured in the sensing equation of motion, as shown in Equations (24) and (26). Figure 11d displays that the SV model predicts a slightly lower optimum load resistance than that computed with the CE models. The OC model does not take the load resistance into account and therefore has no optimum value. The SV and CE models once again agree very well for short-circuit conditions but diverge right about when they reach the optimum load resistance value. On the other hand, for a short-circuit value, the CE-γ diverges but becomes more accurate for load resistances exceeding the optimum load resistance. Similarly, the OC model converges with the SV model as the load resistance is increased.

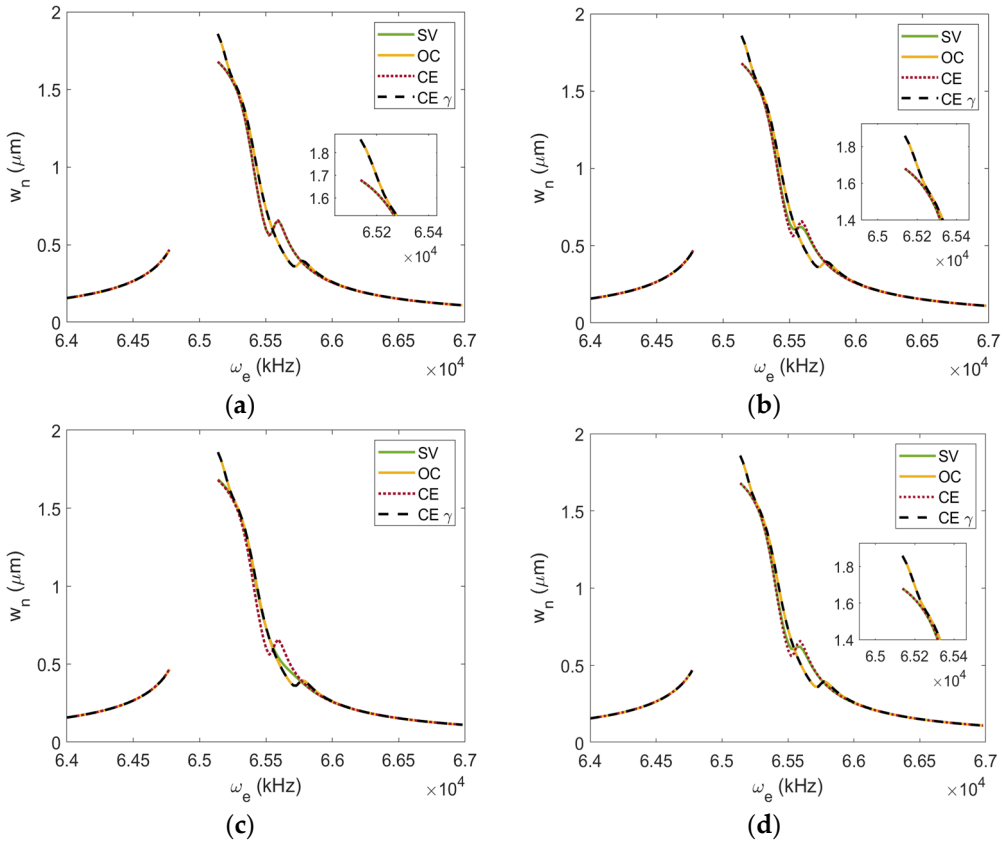

Figure 8. Driving displacement variations as a function of the excitation frequency: (**a**) $R = 10^3\ \Omega$, (**b**) $R = 10^5\ \Omega$, (**c**) $R = \frac{1}{C_p \omega_n}\ \Omega$, and (**d**) $R = 10^8\ \Omega$ when $V_{DC} = 1$ V, V_{AC} = 0.5 V, $\Omega = 80\ \frac{\text{rad}}{\text{s}}$, $\mu = 0.01$.

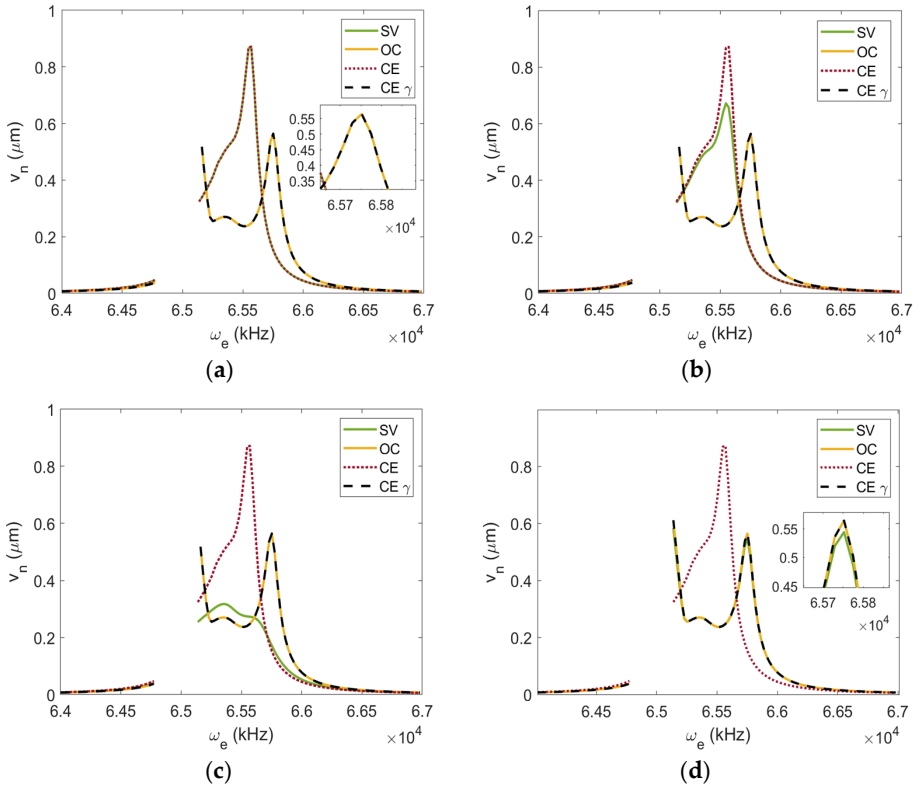

Figure 9. Sensing displacement variations as a function of the excitation frequency: (**a**) $R = 10^3\ \Omega$, (**b**) $R = 10^5\ \Omega$, (**c**) $R = \frac{1}{C_p \omega_n}\ \Omega$, and (**d**) $R = 10^8\ \Omega$ when $V_{DC} = 1$ V, V_{AC} = 0.5 V, $\Omega = 80\ \frac{\text{rad}}{\text{s}}$, $\mu = 0.01$.

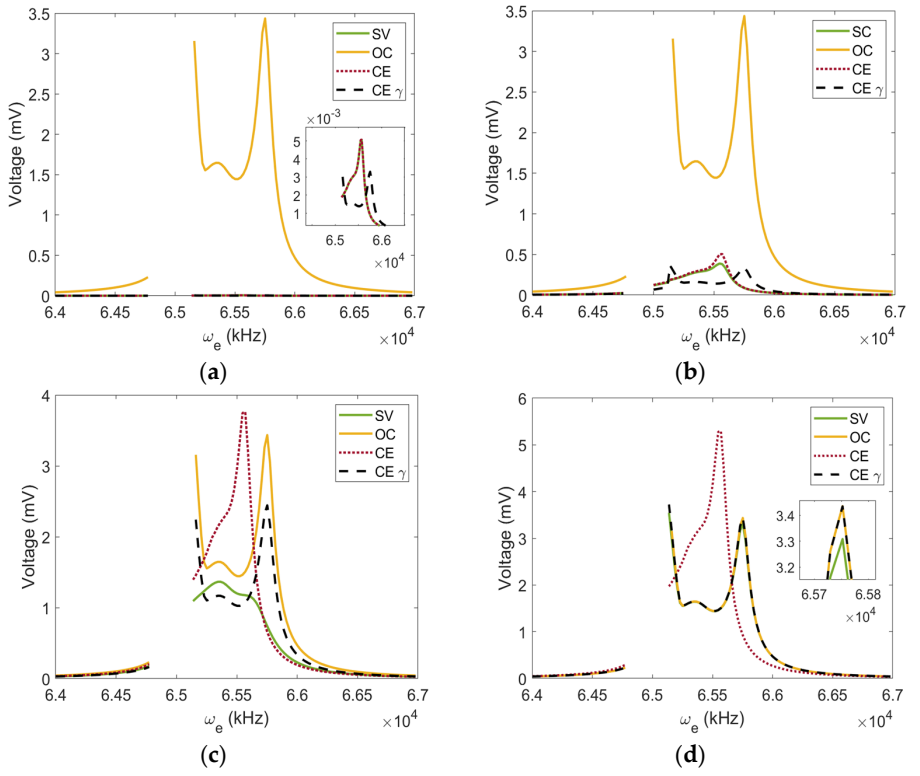

Figure 10. Voltage output variations as a function of the excitation frequency: (**a**) $R = 10^3\ \Omega$, (**b**) $R = 10^5\ \Omega$, (**c**) $R = \frac{1}{C_p \omega_n}\ \Omega$, and (**d**) $R = 10^8\ \Omega$ when $V_{DC} = 1$ V, V_{AC} = 0.5 V, $\Omega = 80\ \frac{\text{rad}}{\text{s}}$, $\mu = 0.01$.

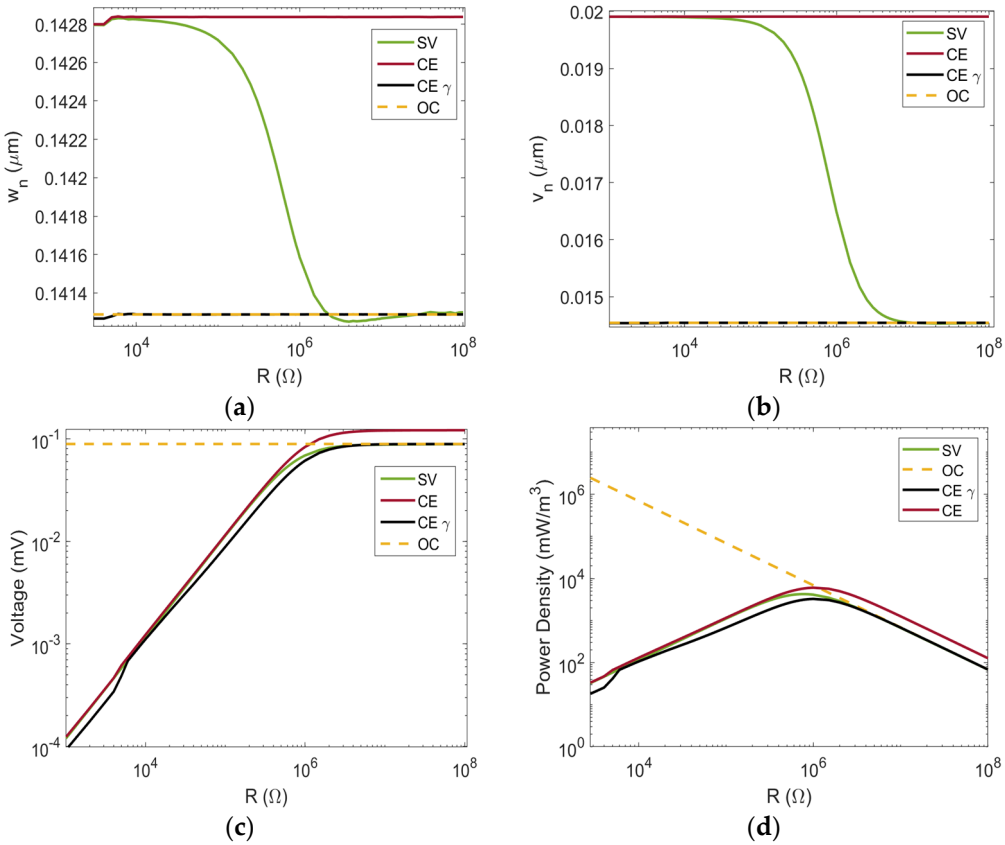

Figure 11. Electrical load resistance effects for various models under consideration: (**a**) driving mode, (**b**) sensing mode, (**c**) generated voltage, and (**d**) power density when $V_{DC} = 1$ V, $V_{AC} = 0.1$ V, $\Omega = 80 \frac{\text{rad}}{\text{s}}$, $\mu = 0.01$.

We proceed with our investigation of the load resistance of multifunctional piezoelectric energy harvesters by tuning the excitation frequency so that it is in resonance with the open-circuit sensing frequency (ω_e = 65,750 Hz), as seen in Figure 12. The same trend that was observed in Figure 11 can be seen. However, there are some distinct differences. One distinction is that the voltage, power density, and sensing displacement for the SV, OC, and CE-γ models are slightly increased. Figure 12a shows another example where the driving displacement for all four models is like that in Figure 11a. Having said that, it should be emphasized that the CE model is still considered viable over a wider range of load resistances. Similarly, the same is true for the OC and CE-γ models. Figure 12b emphasizes that the sensing displacement for the SV model increases as the load resistance increases, in contrast to what is observed in Figure 11b. This occurs because the resonance frequency of the coupled system for lower load resistances is lower than the open-circuit frequency. Therefore, the OC and CE-γ models overestimate the sensing displacement and voltage for lower load resistances. Furthermore, when using the sensing frequency as the excitation frequency, a load resistance higher than $R = 10^8$ Ω is needed for the OC model to converge with the SV model. Figure 12d shows that nearly the same optimum load resistance value (around 10^6 Ω) is obtained for the SV and OC models, while the CE and CE- γ models slightly underestimate the optimum load resistance.

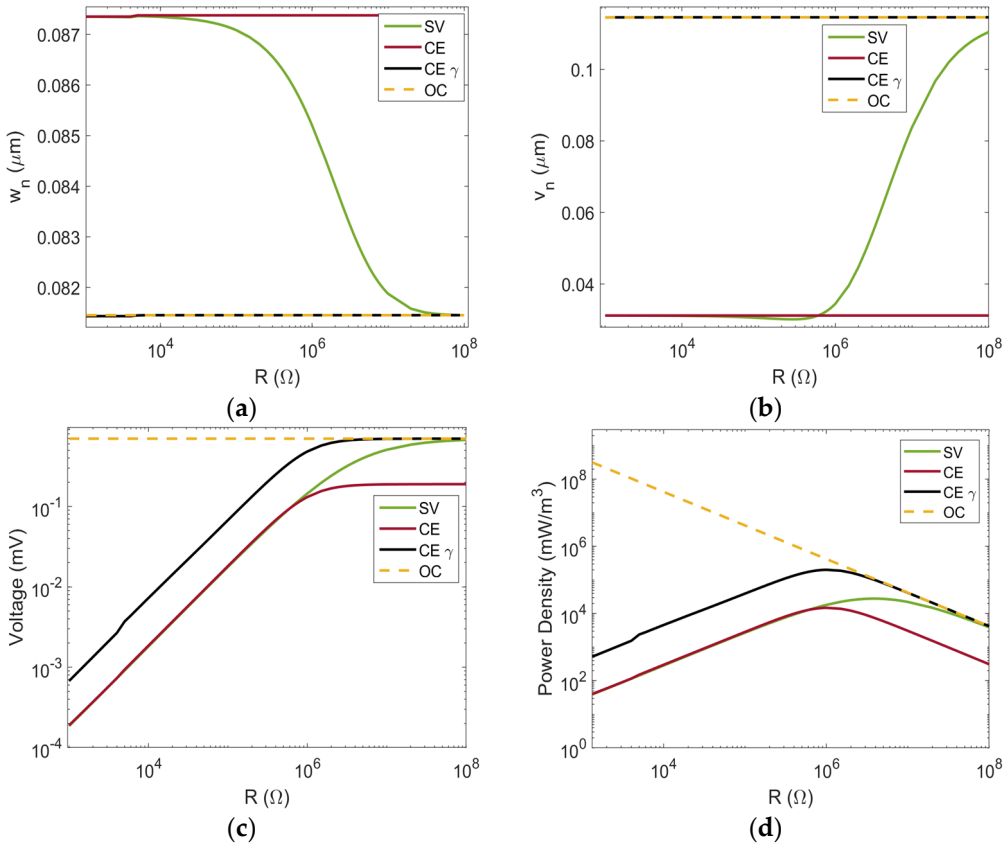

Figure 12. Electrical load resistance effects, near sensing frequency $\omega_e = 65{,}750$ Hz (**a**) driving mode, (**b**) sensing mode, (**c**) harvested voltage, and (**d**) power density when $V_{DC} = 1$ V, $V_{AC} = 0.1$ V, $\Omega = 80 \frac{\text{rad}}{\text{s}}$, $\mu = 0.01$.

The CE-γ model is inaccurate until the load resistance is greater than 10^6 Ω. However, the CE-γ model converges with the SV model at slightly lower values of R than the OC model. This shows the advantage of including additional load resistance-dependent terms in the voltage formulation (Equation (34)). It is noticed that the CE model was unaffected by the sensing displacement, voltage, and power density when using the sensing frequency as the excitation frequency. For high-load resistance, the CE model approximation of voltage and power is less accurate because the excitation frequency is higher than the system's resonance frequency in short circuit.

A properly working gyroscope should be capable of accurate determination of the angular velocity of an object. To accomplish this, it is critical to evaluate the gyroscope's ability to detect changes in the system's base rotation. To investigate this further, the effects of the rotational velocity (at optimum load resistance) on the output voltage as well as the displacements of the driving and sensing modes are explored using the four different models. Using an excitation frequency near the driving resonance frequency, Figure 13 shows graphs of the shifts in driving and sensing positions, as well as the generated voltage responses of the multifunctional gyroscope when the base rotation rate, Ω, is varied. Low DC (1 V) and AC (0.1 V) voltages are selected for the numerical investigation to avoid dynamic pull-in behavior. The driving displacements shown in Figure 13a indicate that for any range of base rotation, Ω, the SV, OC, and CE-γ models are in good agreement, while the CE model only agrees with the other models when the base rotation is less than 100 rad/s. By inspecting the sensing displacements and voltage harvested as shown in Figure 13b,c, the models vary significantly depending on the base rotation value. Table 3 shows the voltage relative error between the OC, CE, and CE-γ models with respect to the SV model for different base rotation values. At low base rotation, the models agree well with one another. However, as the rotation is increased, we observe the appearance

of notable differences between all four models. The OC and CE models remain relatively close to one another until the base rotation gets larger than 200 $\frac{\text{rad}}{\text{s}}$. It is noticed that the CE-γ model has the least relative error for all values of base rotations investigated, while the CE model has the most relative error.

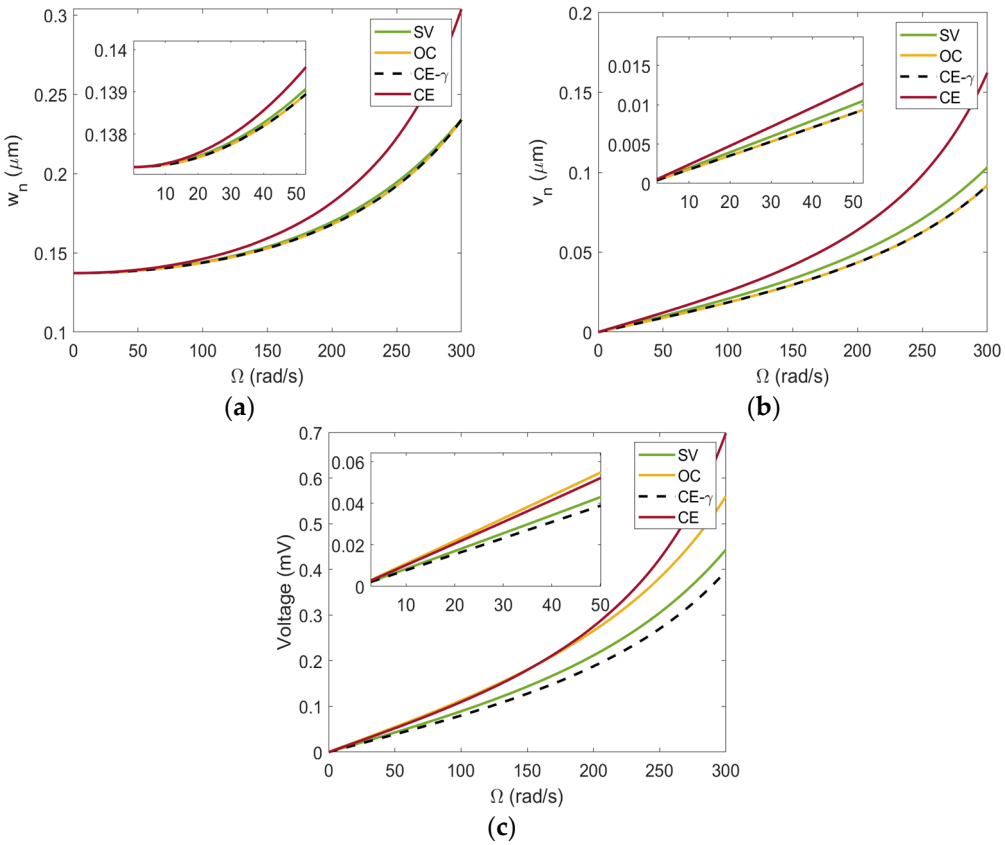

Figure 13. Calibration curves: (**a**) drive displacement, (**b**) sense displacement, (**c**) voltage output when $R = \frac{1}{C_P \omega_e}$, $V_{AC} = 0.1$ V, $V_{DC} = 1$ V, and $\mu = 0.01$.

Table 3. Relative voltage error between SV and other models for different base rotations values.

$\Omega\left(\frac{\text{rad}}{\text{s}}\right)$	OC (V)	CE (V)	CE-γ (V)
15	0.2880	0.2104	0.0854
30	0.2797	0.2112	0.0925
60	0.2712	0.2148	0.0996
90	0.2663	0.2242	0.1038
150	0.2540	0.2540	0.1087
200	0.2547	0.2996	0.1120
250	0.2516	0.3911	0.1145
300	0.2646	0.5764	0.1052

The only valid model at optimal load resistance is the SV model when the system experiences high rotational rates. According to Figure 13, the displacement continues to increase as Ω raises. It can be interpreted that high base rotations are equal to more power. However, when subjected to such high values of base rotation, system fatigue will most likely be reached sooner.

Lastly, a time comparison analysis is performed to determine the difference in numerical expense between the models at different load resistance values. The simulations are run

for one excitation frequency near the driving resonance frequency. We assume 1V DC and 0.1 V AC as well as a damping value of $\mu = 0.01$. The computer used to run the simulations has a clock rate of 1.90 GHz, 16 GB RAM, and a total of 4 cores. Table 4 shows the results of the tests mentioned above. The results indicate that for a low load resistance $R = 10^3\ \Omega$, the fastest model is the OC model requiring only 325 s. However, as stated before, the OC model is not valid under short-circuit conditions. It is worth noting that when load resistance increases, simulation time decreases. For a high-load resistance $R = 10^8\ \Omega$, the difference in simulation time between the models is the smallest. According to the test results, the OC model is preferably the fastest (but only for open-circuit conditions). It is advisable for any other load resistance to using the SV model, especially near the optimum load resistance ($10^5\ \Omega < R < 10^7\ \Omega$). Hybridization between models would be the next step to improve the model even further. Developing one global model that systematically uses the most efficient framework depending on the system load resistance is a topic that must be further investigated.

Table 4. Time variations between models.

Load Resistance	Model	Time (s)	Load Resistance	Model	Time (s)
$R = 10^3$	SV	1653	$R = \frac{1}{C_p \omega_n}\ \Omega$	SV	405
	OC	325		OC	325
	CE-γ	1586		CE-γ	345
	CE	1569		CE	380
$R = 10^5\ \Omega$	SV	415	$R = 10^8\ \Omega$	SV	330
	OC	325		OC	325
	CE-γ	341		CE-γ	343
	CE	393		CE	368

4. Conclusions

Four different methods to model the coupling mechanisms for an energy harvesting microgyroscope system were examined. The simulation results show a comparison between all four models, but the objective is to prove the limits of applicability of each model. A comparison study was conducted to establish the scope of validity for each model. It was discovered that each of the models has an select range of application that is related to the electric load resistance. However, the SV model, which is load resistance dependent, may be used for any load resistance. Only this model was determined to be valid in the vicinity of the optimal load resistance. For energy harvesting purposes, this model is beneficial because it can be trusted at optimum load resistance values. The electrical circuitry needs to be constructed with the optimal load resistance in order to output the highest feasible amount of power, which is important when considering energy harvesting. Only for extremely high-load resistance levels are the OC and CE-γ models considered viable. However, the CE-γ model is the preferred choice for this scenario because it captures some load resistance effects in the voltage equation that are missing in the OC model. Lastly, the CE model is reliable in situations when there is a short circuit, that is, when the load resistance is low. At low load resistances, the use of the SV model is advisable because the difference in simulation time between the CE and SV models is insignificant. Future efforts could employ a hybrid model that combines two or more of these models for use near their applicable load resistance ranges, thus allowing for faster simulation run times. Having accurate mathematical models is the next stage in creating superior energy collecting technologies. When creating new prototypes, this model may be used as a reliable reference point. The model has great promise for directing future experimental observations.

It should be mentioned that as possible future work, techniques such as distribution system reconfiguration can be implemented as one of the most efficient and effective

strategies [63–65] in order to reduce power losses. To this extent, a possible future scope of this work may include the development of a hybrid type model that can change between open- and closed-circuit conditions based on the predetermined load forecasting. It may be possible in a future work to explore the viability of changing models based on the configuration of the electrical circuit. For example, if the circuit was switched to an open-circuit configuration, the OC model may be used. If the switch was closed and a more optimum load resistance is applied the circuit, the SV model should be used for the voltage calculations.

Author Contributions: Conceptualization, M.S., A.A. and S.T.; methodology, M.S., K.L. and A.A.; software, M.S. and K.L.; validation, M.S. and K.L.; formal analysis, M.S., K.L. and A.A.; investigation, M.S., K.L., S.T. and A.A.; resources, M.S., K.L. and A.A.; data curation, M.S.; writing—original draft preparation, M.S.; writing—review and editing, K.L., S.T. and A.A.; visualization, M.S., K.L., S.T. and A.A.; supervision, S.T. and A.A.; project administration, A.A.; funding acquisition, S.T. and A.A. All authors have read and agreed to the published version of the manuscript.

Funding: The authors M. Serrano, S. Tretiak, and A. Abdelkefi gratefully acknowledge the support from the New Mexico Consortium and Los Alamos National Laboratory (LANL).

Data Availability Statement: Data is contained within the article.

Acknowledgments: This work was performed in part at the Center for Integrated Nanotechnology (CINT), a U.S. Department of Energy and Office of Basic Energy Sciences user facility at LANL. K. Larkin acknowledges financial support from the Advanced Simulation and Computing (ASC)—Integrated Codes (IC) Program through the Lagrangian Applications Project at LANL.

Conflicts of Interest: The authors declare no conflict of interest.

References

1. Roundy, S.; Leland, E.S.; Baker, J.; Carleton, E.; Reilly, E.; Lai, E.; Otis, B.; Rabaey, J.M.; Wright, P.K.; Sundararajan, V. Improving power output for vibration-based energy scavengers. *IEEE Pervasive Comput.* **2005**, *4*, 28–36. [CrossRef]
2. Kumar, R.; Pachauri, R.K.; Badoni, P.; Bharadwaj, D.; Mittal, U.; Bisht, A. Investigation on parallel hybrid electric bicycle along with issuer management system for mountainous region. *J. Clean. Prod.* **2022**, *362*, 132430. [CrossRef]
3. Kumar, R.; Kumar, A. Nature based self-learning mechanism and simulation of automatic control smart hybrid antilock braking system. *Wirel. Pers. Commun.* **2021**, *116*, 3291–3308. [CrossRef]
4. Elahi, H.; Eugeni, M.; Gaudenzi, P. A review on mechanisms for piezoelectric-based energy harvesters. *Energies* **2018**, *11*, 1850. [CrossRef]
5. Cook-Chennault, K.A.; Thambi, N.; Sastry, A.M. Powering MEMS portable devices—A review of non-regenerative and regenerative power supply systems with special emphasis on piezoelectric energy harvesting systems. *Smart Mater. Struct.* **2008**, *17*, 043001. [CrossRef]
6. Wei, S.; Hu, H.; He, S. Modeling and experimental investigation of an impact-driven piezoelectric energy harvester from human motion. *Smart Mater. Struct.* **2013**, *22*, 105020. [CrossRef]
7. Najini, H.; Muthukumaraswamy, S.A. Investigation on the selection of piezoelectric materials for the design of an energy harvester system to generate energy from traffic. *Int J. Eng. Appl. Sci.* **2016**, *3*, 257722.
8. Elvin, N.G.; Elvin, A.A. An experimentally validated electromagnetic energy harvester. *J. Sound Vib.* **2011**, *330*, 2314–2324. [CrossRef]
9. Zhou, N.; Gao, S.; Li, R.; Ao, H.; Jiang, H. Transient output performance of symmetrical V-shaped micro-piezoelectric energy harvester by using PZT-5H. *Microsyst. Technol.* **2021**, *27*, 779–787. [CrossRef]
10. Pozzi, M.; Aung, M.S.; Zhu, M.; Jones, R.K.; Goulermas, J.Y. The pizzicato knee-joint energy harvester: Characterization with biomechanical data and the effect of backpack load. *Smart Mater. Struct.* **2012**, *21*, 075023. [CrossRef]
11. Salazar, R.; Serrano, M.; Abdelkefi, A. Fatigue in piezoelectric ceramic vibrational energy harvesting: A review. *Appl. Energy* **2020**, *270*, 115161. [CrossRef]
12. Yin, Z.; Gao, S.; Jin, L.; Sun, Y.; Wu, Q.; Zhang, X.; Guo, S. A dual impact driven frequency up-conversion piezoelectric energy harvester for ultralow-frequency and wide-bandwidth operation. *Sens. Actuators A Phys.* **2021**, *331*, 112961. [CrossRef]
13. Liang, F.; Liang, D.-D.; Qian, Y.-J. Dynamical analysis of an improved MEMS ring gyroscope encircled by piezoelectric film. *Int. J. Mech. Sci.* **2020**, *187*, 105915. [CrossRef]
14. Lu, H.; Chai, T.; Cooley, C.G. Vibration properties of a rotating piezoelectric energy harvesting device that experiences gyroscopic effects. *J. Sound Vib.* **2018**, *416*, 258–278. [CrossRef]
15. Pillatsch, P.; Yeatman, E.M.; Holmes, A.S. A piezoelectric frequency up-converting energy harvester with rotating proof mass for human body applications. *Sens. Actuators A Phys.* **2014**, *206*, 178–185. [CrossRef]

16. Chen, C.; Xu, T.-B.; Yazdani, A.; Sun, J.-Q. A high density piezoelectric energy harvesting device from highway traffic—System design and road test. *Appl. Energy* **2021**, *299*, 117331. [CrossRef]
17. Fan, Y.; Ghayesh, M.H.; Lu, T.-F. High-efficient internal resonance energy harvesting: Modelling and experimental study. *Mech. Syst. Signal Process.* **2022**, *180*, 109402. [CrossRef]
18. Karmakar, D.; Majumdar, K.; Pal, M.; Roy, P.K.; Machavarapu, S. Energy harvesting from pedestrian movement using piezoelectric material. *Mater. Today Proc.* **2021**, *57*, 391–397. [CrossRef]
19. Chen, C.; Sharafi, A.; Sun, J.-Q. A high density piezoelectric energy harvesting device from highway traffic–Design analysis and laboratory validation. *Appl. Energy* **2020**, *269*, 115073. [CrossRef]
20. Tan, T.; Zuo, L.; Yan, Z. Environment coupled piezoelectric galloping wind energy harvesting. *Sens. Actuators A Phys.* **2021**, *323*, 112641. [CrossRef]
21. Yang, K.; Su, K.; Wang, J.; Wang, J.; Yin, K.; Litak, G. Piezoelectric wind energy harvesting subjected to the conjunction of vortex-induced vibration and galloping: Comprehensive parametric study and optimization. *Smart Mater. Struct.* **2020**, *29*, 075035. [CrossRef]
22. Jia, J.; Shan, X.; Upadrashta, D.; Xie, T.; Yang, Y.; Song, R. Modeling and analysis of upright piezoelectric energy harvester under aerodynamic vortex-induced vibration. *Micromachines* **2018**, *9*, 667. [CrossRef] [PubMed]
23. Wang, Q.; Ruan, T.; Xu, Q.; Yang, B.; Liu, J. Wearable multifunctional piezoelectric MEMS device for motion monitoring, health warning, and earphone. *Nano Energy* **2021**, *89*, 106324. [CrossRef]
24. Lee, M.-S.; Kim, C.-I.; Park, W.-I.; Cho, J.-H.; Paik, J.-H.; Jeong, Y.H. Energy harvesting performance of unimorph piezoelectric cantilever generator using interdigitated electrode lead zirconate titanate laminate. *Energy* **2019**, *179*, 373–382. [CrossRef]
25. Naseer, R.; Dai, H.; Abdelkefi, A.; Wang, L. Comparative study of piezoelectric vortex-induced vibration-based energy harvesters with multi-stability characteristics. *Energies* **2020**, *13*, 71. [CrossRef]
26. Wang, S.; Liao, W.; Zhang, Z.; Liao, Y.; Yan, M.; Kan, J. Development of a novel non-contact piezoelectric wind energy harvester excited by vortex-induced vibration. *Energy Convers. Manag.* **2021**, *235*, 113980. [CrossRef]
27. Bai, Y.; Jantunen, H.; Juuti, J. Energy harvesting research: The road from single source to multisource. *Adv. Mater.* **2018**, *30*, 1707271. [CrossRef] [PubMed]
28. Sirohi, J.; Mahadik, R. Harvesting wind energy using a galloping piezoelectric beam. *J. Vib. Acoust.* **2011**, *134*, 011009. [CrossRef]
29. Abdelkefi, A.; Hajj, M.; Nayfeh, A. Piezoelectric energy harvesting from transverse galloping of bluff bodies. *Smart Mater. Struct.* **2012**, *22*, 015014. [CrossRef]
30. Jang, J.; Hwang, G.-T.; Min, Y.; Kim, J.-W.; Ahn, C.-W.; Choi, J.-J.; Hahn, B.-D.; Choi, J.-H.; Park, D.-S.; Jung, Y.; et al. Fatigue study and durability improvement of piezoelectric single crystal macro-fiber composite energy harvester. *J. Korean Ceram. Soc.* **2020**, *57*, 645–650. [CrossRef]
31. Abdelkefi, A.; Yan, Z.; Hajj, M.R. Modeling and nonlinear analysis of piezoelectric energy harvesting from transverse galloping. *Smart Mater. Struct.* **2013**, *22*, 025016. [CrossRef]
32. Nayfeh, A.H.; Balachandran, B. *Applied Nonlinear Dynamics: Analytical, Computational, and Experimental Methods*; John Wiley & Sons: Hoboken, NJ, USA, 2008.
33. Alghisi, D.; Dalola, S.; Ferrari, M.; Ferrari, V. Triaxial ball-impact piezoelectric converter for autonomous sensors exploiting energy harvesting from vibrations and human motion. *Sens. Actuators A Phys.* **2015**, *233*, 569–581. [CrossRef]
34. Minami, Y.; Nakamachi, E. Development of enhanced piezoelectric energy harvester induced by human motion. In Proceedings of the 2012 Annual International Conference of the IEEE Engineering in Medicine and Biology Society, San Diego, CA, USA, 28 August–1 September 2012; IEEE: Manhattan, NY, USA, 2012; pp. 1627–1630.
35. Halim, M.A.; Khym, S.; Park, J.Y. Impact based frequency increased piezoelectric vibration energy harvester for human motion related environments. In Proceedings of the 8th Annual IEEE International Conference on Nano/Micro Engineered and Molecular Systems, Suzhou, China, 7–10 April 2013; IEEE: Manhattan, NY, USA, 2013; pp. 949–952.
36. Yang, B.; Yun, K.-S. Efficient energy harvesting from human motion using wearable piezoelectric shell structures. In Proceedings of the 2011 16th International Solid-State Sensors, Actuators and Microsystems Conference, Beijing, China, 5–9 June 2011; IEEE: Manhattan, NY, USA, 2011; pp. 2646–2649.
37. Qian, F.; Xu, T.-B.; Zuo, L. Piezoelectric energy harvesting from human walking using a two-stage amplification mechanism. *Energy* **2019**, *189*, 116140. [CrossRef]
38. Ghommem, M.; Nayfeh, A.; Choura, S.; Najar, F.; Abdel-Rahman, E. Modeling and performance study of a beam microgyroscope. *J. Sound Vib.* **2010**, *329*, 4970–4979. [CrossRef]
39. Liu, Z.; Zhang, S.; Jim, Y.M.; Ouyang, H.; Zou, Y.; Wang, Y.X.; Xie, L.X.; Li, Z. Flexible piezoelectric nanogenerator in wearable self-powered active sensor for respiration and healthcare monitoring. *Semicond. Sci. Technol.* **2017**, *32*, 064004. [CrossRef]
40. Chandrasekaran, S.; Bowen, C.; Roscow, J.; Zhanf, Y.; Danf, D.K.; Kim, E.J.; Misra, R.D.K.; Deng, L.; Chung, J.S.; Hur, S.H. Micro-scale to nano-scale generators for energy harvesting: Self powered piezoelectric, triboelectric and hybrid devices. *Phys. Rep.* **2019**, *792*, 1–33. [CrossRef]
41. Mokhtari, F.; Spinks, G.M.; Fay, C.; Cheng, Z.; Raad, R.; Xi, J.; Foroughi, J. Wearable electronic textiles from nanostructured piezoelectric fibers. *Adv. Mater. Technol.* **2020**, *5*, 1900900. [CrossRef]
42. Bellman, R.; Kusanagi, M. Methods of Nonlinear Analysis, Vol. I (Mathematics in Science and Engineering Volume 61-I). *J. Dyn. Syst. Meas. Control* **1973**, *95*, 103–104. [CrossRef]

43. Biswal, P.; Kar, S.K.; Mukherjee, B. Design and optimization of high-performance through hole based MEMS energy harvester using PiezoMUMPs. *J. Electron. Mater.* **2021**, *50*, 375–388. [CrossRef]
44. Naval, S.; Sinha, P.K.; Das, N.K.; Anand, A.; Kundu, S. Wideband piezoelectric energy harvester design using parallel connection of multiple beams. *Int. J. Nanopart.* **2020**, *12*, 206–223. [CrossRef]
45. Panayanthatta, N.; La Rosa, R.; Trigona, C.; Bano, E.; Montes, L. Optimization of the geometry of MEMS Piezoelectric Energy Harvester cantilevers. In Proceedings of the COMSOL Conference Europe 2020, Cambridge, UK, 14–15 October 2020.
46. Larkin, K.; Ghommem, M.; Serrano, M.; Abdelkefi, A. A review on vibrating beam-based micro/nano-gyroscopes. *Microsyst. Technol.* **2021**, *27*, 4157–4181. [CrossRef]
47. Zhang, Y.-W.; Su, C.; Ni, Z.-Y.; Zang, J.; Chen, L.-Q. A multifunctional lattice sandwich structure with energy harvesting and nonlinear vibration control. *Compos. Struct.* **2019**, *221*, 110875. [CrossRef]
48. Brito-Pereira, R.; Ribeiro, C.; Pereira, N.; Lanceros-Mendez, S.; Martins, P. Printed multifunctional magnetically activated energy harvester with sensing capabilities. *Nano Energy* **2022**, *94*, 106885. [CrossRef]
49. Cho, J.Y.; Kim, K.-B.; Hwang, W.S.; Yang, C.H.; Ahn, J.H.; Hong, S.D.; Jeon, D.H.; Song, G.J.; Ryu, C.H.; Woo, S.B.; et al. A multifunctional road-compatible piezoelectric energy harvester for autonomous driver-assist LED indicators with a self-monitoring system. *Appl. Energy* **2019**, *242*, 294–301. [CrossRef]
50. Bellman, R.; Adomian, G. *Partial Differential Equations*; D. Reidel Publishing: Dordrecht, The Netherlands, 1985.
51. Bellman, R.; Roth, R. *Methods in Approximation*; D. Reidel Publishing: Dordrecht, The Netherlands, 1986.
52. Bert, C.W.; Malik, M. *Differential Quadrature Method in Computational Mechanics: A Review*; Springer: London, UK, 1996.
53. Nayak, M.; Wakif, A.; Animasaun, I.; Alaoui, M. Numerical Differential Quadrature Examination of Steady Mixed Convection Nanofluid Flows Over an Isothermal Thin Needle Conveying Metallic and Metallic Oxide Nanomaterials: A Comparative Investigation. *Arab. J. Sci. Eng.* **2020**, *45*, 5331–5346. [CrossRef]
54. Wang, J.; Geng, L.; Zhou, S.; Zhang, Z.; Lai, Z.; Yurchenko, D. Design, modeling and experiments of broadband tristable galloping piezoelectric energy harvester. *Acta Mech. Sin.* **2020**, *36*, 592–605. [CrossRef]
55. Mohammadimehr, M.; Mehrabi, M.; Mousavinejad, F.S. Magneto-mechanical vibration analysis of single-/three-layered micro-Timoshenko porous beam and graphene platelet as reinforcement based on modified strain gradient theory and differential quadrature method. *J. Vib. Control* **2020**, *27*, 1077546320949083. [CrossRef]
56. Larkin, K.; Ghommem, M.; Abdelkefi, A. Significance of size dependent and material structure coupling on the characteristics and performance of nanocrystalline micro/nano gyroscopes. *Phys. E Low-Dimens. Syst. Nanostruct.* **2018**, *99*, 169–181. [CrossRef]
57. Serrano, M.; Larkin, K.; Ghommem, M.; Tretiak, S.; Abdelkefi, A. Broadband piezoelectric energy harvesting microgyroscopes: Design and nonlinear analysis. *Eur. J. Mech. A Solids* **2022**, *98*, 104888. [CrossRef]
58. Abdelkefi, A.; Barsallo, N. Comparative modeling of low-frequency piezomagnetoelastic energy harvesters. *J. Intell. Mater. Syst. Struct.* **2014**, *25*, 1771–1785. [CrossRef]
59. Aridogan, U.; Basdogan, I.; Erturk, A. Analytical modeling and experimental validation of a structurally integrated piezoelectric energy harvester on a thin plate. *Smart Mater. Struct.* **2014**, *23*, 045039. [CrossRef]
60. Wu, H.; Tang, L.; Yang, Y.; Soh, C.K. Development of a broadband nonlinear two-degree-of-freedom piezoelectric energy harvester. *J. Intell. Mater. Syst. Struct.* **2014**, *25*, 1875–1889. [CrossRef]
61. Erturk, A. *Electromechanical Modeling of Piezoelectric Energy Harvesters*; Virginia Tech: Blacksburg, VA, USA, 2009.
62. Larkin, K.; Abdelkefi, A. Neutral axis modeling and effectiveness of functionally graded piezoelectric energy harvesters. *Compos. Struct.* **2019**, *213*, 25–36. [CrossRef]
63. Mahdavi, M.; Alhelou, H.H.; Hesamzadeh, M.R. An efficient stochastic reconfiguration model for distribution systems with uncertain loads. *IEEE Access* **2022**, *10*, 10640–10652. [CrossRef]
64. Macedo, L.H.; Franco, J.F.; Mahdavi, M.; Romero, R. A contribution to the optimization of the reconfiguration problem in radial distribution systems. *J. Control Autom. Electr. Syst.* **2018**, *29*, 756–768. [CrossRef]
65. Hosseini, H.; Jalilzadeh, S.; Nabaei, V.; Govar, G.Z.; Mahdavi, M. Enhancing deregulated distribution network reliability for minimizing penalty cost based on reconfiguration using BPSO. In Proceedings of the 2008 IEEE 2nd International Power and Energy Conference, Johor Bahru, Malaysia, 1–3 December 2008; IEEE: Manhattan, NY, USA, 2008; pp. 983–987.